Covalent bond inducing strong electron-phonon coupling superconductivity in MgB_2-type transition metal diboride WB_2

Jiajun Wang,[1,2] Muyao Wang,[2] Xiaohan Liu,[2] Man Jiang,[3,*] and Liangliang Liu[2,†]

[1]*SDU-ANU Joint Science College, Shandong University, Weihai, Shandong 264209, People's Republic of China*

[2]*Key Laboratory for Special Functional Materials of Ministry of Education, School of Materials Science and Engineering, Henan University, Kaifeng 475004, People's Republic of China*

[3]*Department of Nuclear Engineering and Technology, School of Energy and Power Engineering, Huazhong University of Science and Technology, Wuhan 430073, People's Republic of China*

(Received 22 March 2023; revised 28 June 2023; accepted 29 June 2023; published 19 July 2023)

A recent experiment of polycrystalline WB_2 with hP3 (space-group 191, prototype MgB_2) and hP12 (space-group 194, prototype WB_2) structures was reported to realize 17-K superconductivity (SC) at 90 GPa, and the hP3 structure is believed to be responsible for this emergent SC. However, a microscopic understanding of what makes the hP3 structure so different from the hP12 structure and why the hP3 can feature such strong electron-phonon coupling (EPC) SC is still missing. Here, based on first-principles calculations, we found that in the hP3 structure, W d orbitals contribute most to electronic occupation near the E_F, and d_{z^2} orbitals of two neighboring W atoms have some hybridization to form weak σ bonds. The further EPC analysis indicates that the dominant d_{z^2} states are strongly coupled with the out-of-plane phonon modes by stretching the W-Wσ bond, thereby yielding a large superconducting gap and high T_c of ∼35 K. By contrast, for the hP12 structure, two neighboring W atoms are isolated without charge hybridization to form the covalent bonds, and, accordingly, their phonon modes become very stiffened, which cannot effectively couple to W d orbital states associated with a lower T_c of ∼4 K. Therefore, our findings not only provide an explanation for the emergent strong EPC SC in the hP3 structure, but also have important implications for the design of high-T_c superconductors among transition metal borides.

DOI: 10.1103/PhysRevMaterials.7.074804

I. INTRODUCTION

Hexagonal layered MgB_2, discovered by Akimitsu and co-workers in 2001, is a well-known phonon-mediated superconductor with a transition temperature T_c ∼ 39 K [1], and the B-B σ-bonding state was demonstrated to play a central role in the superconducting pair via coupling with the in-plane stretching modes of the B layer [2–8]. Subsequently, a great deal of effort has been devoted into searching for and designing more boride superconductors in order to obtain higher T_c by substituting Mg atoms or partially doping other elements into MgB_2 experimentally and theoretically [9–12]. For instance, a well-known case is CaB_2, and theory predicted that isostructural CaB_2 hosts the stronger electron-phonon coupling (EPC) than that of MgB_2 with T_c up to 48 K [13], whereas, unfortunately, it is difficult for experiment to synthesize due to the poor thermodynamic stability. Doping with Ba in MgB_2, the obtained $Mg_{0.5}Ba_{0.5}B_2$ was predicted to have superconductivity (SC) at the ∼60 K [14], and we are not aware of experimental progress on this prediction. To date, as we know, MgB_2 remains to host the experimentally confirmed the highest T_c among all boride superconductors.

Recently, Pei *et al.* carried out the high-pressure experiment to explore the SC of transition diboride MoB_2 and found high pressure drives it from the $R\bar{3}m$ phase transition into $P6/mmm$ phase, which exhibits very strong EPC SC with T_c up to ∼32 K under 90 GPa [15,16]. Inspired by the experimental finding of MoB_2 SC, more recently, Lim *et al.* [17] and Pei *et al.* [18] also study the superconductivity of isoelectronic compound WB_2 under pressure, respectively. Lim synthesized large-grain polycrystalline WB_2 samples with hP3 ($P6/mmm$) and hP12 ($P6_3/mmc$) structures, and under the combined effect of these two structures at the grain boundary, the obtained T_c is ∼17 K at 90 GPa [17]. The detailed analysis implies that the hP3 structure, the isostructure to MgB_2, was believed to play a key role in the emergency of the 17-K SC for polycrystalline WB_2 since the hP3 structure was theoretically predicted to have T_c of 25–40 K, whereas, the T_c of $P6_3/mmc$ phase is only ∼1 K [17,19]. However, a microscopic understanding of what makes the hP3 structure so different from the hP12 structure and why the hP3 can feature such high T_c is still missing. It is, therefore, necessary to investigate the salient electronic, bonding, and phononic properties of the hP3 and hP12 structures from which large EPC is derived.

In this paper, first-principles calculation within the anisotropic Migdal-Eliashberg (M-E) theory [20,21] was carried out to study the superconducting mechanism of hP3 and hP12 structures. It is found that, in the hP3 structure, W d orbitals have the large electronic occupation near the E_F, and

*Corresponding author: jiangm@hust.edu.cn
†Corresponding author: liull@henu.edu.cn

especially d_{z^2} orbitals of two neighboring W atoms have some hybridization, forming the weak σ bonds. The detailed EPC analysis indicates that the dominant d_{z^2} states are strongly coupled with the out-of-plane phonon modes by stretching the W-Wσ bond, giving rise to a large superconducting gap of 8 meV, and, thus, obtaining T_c up to ~35 K. Although for the hP12 structure, two neighboring W atoms are isolated without charge hybridization to form the covalent bonds, and accordingly their phonon vibrations get very stiffened, which cannot effectively couple with W d states associated with obtaining a low T_c of 4 K. Doubtlessly, our present findings not only elucidate the microscopic mechanism of the emergent high T_c in the hP3 structure, but also provide a guidance to design more high-T_c boride superconductors.

II. CALCULATIONAL METHODS

Our density functional theory (DFT) calculations were performed using the Vienna *ab initio* simulation package with the projector augmented-wave method [22–24]. The generalized-gradient approximation functional of Perdew-Burke-Ernzerhof (PBE) [25] was used to deal with the exchange-correlation energy, and a plane-wave basis was taken with a kinetic-energy cutoff of 600 eV. The **k**-space integration was performed with 21^3 ($21 \times 21 \times 7$) k-point grid for the hP3 (hP12) structure optimization, and all atoms were allowed to relax along the calculated forces until all the residual force components were less than 0.005 eV/Å. The subsequent lattice dynamics and EPC calculations were carried out by using the QUANTUM ESPRESSO (QE) package [26] with the optimized norm-conserving Vanderbilt pseudopotentials [27] and a plane-wave cutoff of 80 Ry. Here, we used 6^3 ($6 \times 6 \times 4$) q-point grid for the phonon computation of the hP3 (hP12) structure. The anisotropic M-E equations with a typical Coulomb pseudopotential parameter of μ= 0.13 and 0.15 [15,28] are employed to calculate the superconducting gap and estimate the T_c as implemented in the electron-phonon Wannier (EPW) code [29], and the interpolated k-point grid of $50 \times 50 \times 40$ and q-point grid of $25 \times 25 \times 20$ are used in the superconducting calculations.

III. RESULTS

We first begin by optimizing the hP3 WB_2 structure using the PBE calculations. Figures 1(a) and 1(b) show the optimized structure at 90 GPa, and the obtained lattice parameters are $a = b = 2.857$ Å and $c = 3.117$ Å, respectively. In the bulk structure, W atoms are intercalated between two B-B layers, occupied at the honeycomb center. Based on the crystal-field analysis (W site: D_{6h} point group), W 5d orbitals can be splitted into a singlet a_{1g} (d_{z^2}), and two doublets e_{1g} (d_{xy} and d_{yz}) and e_{2g} (d_{xy} and $d_{x^2-y^2}$). The calculated projected band structure (Pband) is shown in Fig. 1(c). It is seen that there are four bands (denoted as n = 1–4) across the E_F, and W d orbitals contribute most to the electronic states at the E_F. Compared with other orbitals, the singlet d_{z^2} orbital is the most dominant component of the states, which has some hybridization to the B p_z orbitals along the k-path L-V-N-K with a relatively small energetic dispersion, and, thus, to form double Van Hove singularities (VHSs) associated with two

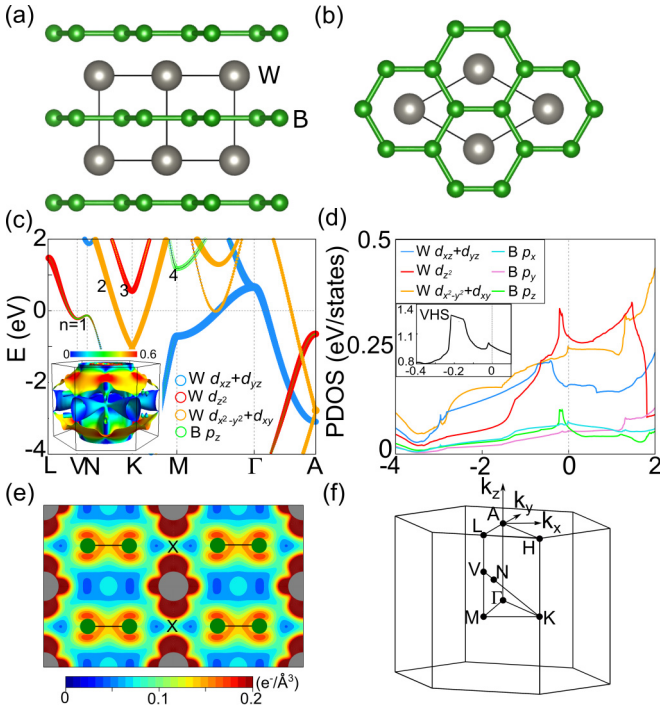

FIG. 1. (a) Side view and (b) top view of the hP3 structure under 90 GPa. (c) Calculated band structure with projected onto the atomic orbitals. The inset of (c) is the distribution of d_{z^2} states on the Fermi surface (FS) using the color scale in the range of [0, 0.6]. (d) Partial density of state (PDOS). A closeup of the total DOS around the E_F is given in the inset of (d). (e) Calculated partial charge density plotted on the (110) surface of the 2^3 supercell. The center of the σ bonds between two neighboring W atoms are marked by "X." (f) Brillouin zone of the primitive cell.

large localized peaks in the DOS below the E_F [see Figs. 1(c) and 1(d)]. It is noted that such double VHSs are also observed in the isostructural MoB_2 [16]. Figure 1(c) displays the projected states of the dominant d_{z^2} orbital on the FS sheets, which are extensively distributed on the FS sheet of the band n=1, exhibiting anisotropic distribution.

In the following, we plot the partial charge density distribution in the range from −0.1 to 0.1 eV [see Fig. 1(e)] since the formation of Cooper pairs are just related to the electronic charges near the E_F. It is displayed that the charges are mainly located around W atoms, and the d_{z^2} orbitals of two neighboring W atoms have some hybridization to be connected by weak σ bonds, having a saddle point of charge density at this middle with value of 0.10 e^-/Å^3. This W-W σ bond is also confirmed by the calculated crystal orbital Hamiltonian population (COHP) [30–32] in Fig. 2(a) shows that the COHP curve for the neighboring W-W is negative below the E_F, and the integrated COHP up to E_F is −0.86 eV/pair, clearly indicating there are bonding states between two neighboring W atoms. Meanwhile, as the pressure increases, Fig. 2(b) shows the values of integrated COHP are increased and accordingly the strength of the W-W σ bond gets an enhancement. Additionally, it is noteworthy that this d_{z^2} driven-σ bond is also observed between two neighboring Mo atoms of the MoB_2 with the hP3 structure under high pressure, and since the isoelectronic compounds WB_2 and MoB_2 exhibit the

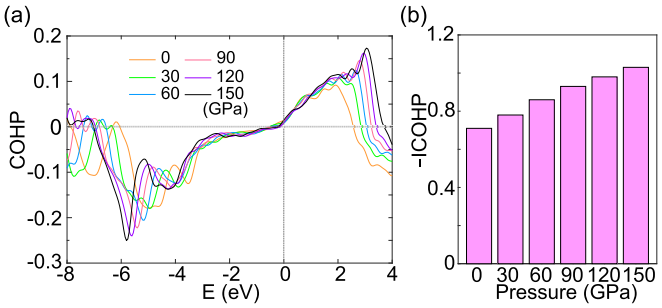

FIG. 2. (a) The calculated projected COHP for the two neighboring W atoms evolve as a function of pressure. (b) The corresponding values of integrated COHP at different pressures. Here, a negative COHP indicates bonding states and positive COHP indicates antibonding states.

similar band structure, electronic DOS, and bonding nature (see Figs. 1 and 2 of Ref. [15]), naturally, they would have the similar phonon vibrations, EPC, and SC as discussed below.

We then turn to examine the phonon modes and EPC of the hP3 structure using the density functional perturbation theory calculation [38]. Figure 3(a) shows the atom-mode projected phonon spectrum. It is revealed that there is a small gap of ∼25 meV between high-frequency optical branches and low-frequency acoustic branches. The optical branches almost come from the contribution of the B vibration. We note that because the B p orbitals are mainly located at the low-energy level and have low electronic occupation near the

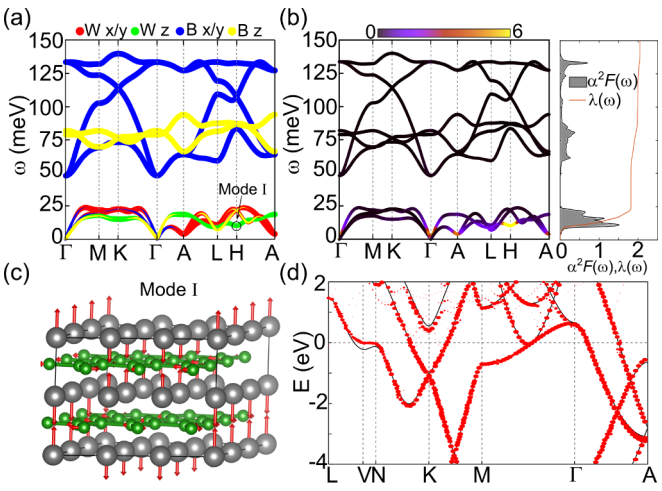

FIG. 3. (a) Phonon spectrum projected on atomic in-plane (x/y) and out-of-plane (z) vibrations. (b) Phonon spectrum with projection of EPC strength λ_{qv} using the color scale in the range of [0,6], and the isotropic Eliashberg function $\alpha^2F\omega$ with integrated EPC constant $\lambda(\omega)$. (c) Atomic displacements of e mode I, labeled as indicated in (a). Here, since mode I corresponds to the q-point coordinate of about number $(\frac{1}{3}, \frac{1}{3}, \frac{1}{2})$, a $3 \times 3 \times 2$ supercell was employed to fold this q point into the Brillouin-zone center. The arrows on W/B atoms indicate vibrational directions. (d) The unfolding band structure (red points) with the atomic displacements of mode I, plotted along the same k path of equilibrium structure in the primitive cell (bottom black lines) to facilitate comparison.

E_F, these B vibration modes cannot effectively coupled with B electronic states, and the obtained q-vector EPC parameters $\lambda_{q,v}$ are all very small [see Fig. 3(b)]. By contrast, the low-frequency acoustic modes driven by W vibrations give rise to the large EPC strength. Especially, along the q-path A-L-H, the W out-of-plane vibrations experience a sharp softening, and the corresponding mode I produces the strongest EPC by stretching and compressing the weak W-W σ bonds along the z direction [see Figs. 3(b) and 3(c)]. This is further identified by the fact that the d_{z^2}-driven band across the E_F, e.g., states near the VHS, obviously moves up as the W atomic displacements according to the unfolding band dispersion in Fig. 3(d). The underlying physics is that if a phonon can be strongly coupled with FS states, it will produce a large energetic shift in k for states near E_F [39].

Next, in order to quantitatively evaluate the EPC strength, we further calculated the isotropic Eliashberg spectral function $\alpha^2F(\omega)$ to obtain the total EPC constant λ based on Eq. [40]: $\lambda(\omega) = 2\int_0^\omega d\omega\, \alpha^2F(\omega)/\omega$. The calculated total λ value is 2.02. From Fig. 3(b), it is found that the $\alpha^2F(\omega)$ exhibits a huge peak around the low-frequency region derived by W phonon modes, yielding a sharp increase in $\lambda(\omega)$, and integrating the contribution of three acoustic phonon branches, the obtained λ value is 1.85, occupying more than 90% of the total λ, indicating that the emergent strong EPC almost come from the contribution of the acoustic branches.

Since there typically exist several bands crossing E_F and atomic orbitals exhibit the anisotropic distribution on the FS, here, the anisotropic M-E equations were used to evaluate the **k**-resolved EPC parameter λ_{nk} to reflect the coupling strength of the phonons with each electron band and the anisotropic nature of superconducting gap Δ_{nk} as employed in MgB_2 superconducting analysis [4], and the tight-binding Hamiltonian with the maximally localized Wannier function reproduces well the electronic bands obtained using the DFT calculation [see Fig. S1 of Supplemental Material [33]] as implemented in the EPW code. Figures 4(a) and 4(b) show the distribution of λ_{nk} and Δ_{nk} on the FS. It is noted that the λ_{nk} strength on the FS exhibits significant anisotropy and are scaled with the weight of W d_{z^2} states on the FS. Accordingly, the W d_{z^2} states on the FS give rise to the large superconducting gap Δ_{nk}, and noted that Δ_{nk}'s are closely correlated with λ_{nk}, i.e., the larger Δ_{nk} strength, the higher Δ_{nk}. Then, normalized quasiparticle DOSs was calculated to compare with the experimental tunneling conductance directly based on the $\frac{N_S(\omega)}{N_F} = \mathrm{Re}[\frac{\omega}{\sqrt{\omega^2-\Delta^2(\omega)}}]$ [41]. Figure 4(c) shows there is only a pair of peaks, corresponding to a single superconducting gap. As the increase of temperature T, the value of gap gradually decreases to zero at the ∼35 K using the $\mu^* = 0.13$, and, thus, the obtained T_c of the hP3 structure is 35 K [see Fig. 4(d)]. If $\mu^* = 0.15$ was used to calculate T_c, and the value is ∼30 K. Therefore, the estimated T_c of the hP3 structure is located 30–35 K with $\mu^* = 0.13$–0.15. The similar superconducting nature also happens in MoB_2 that d_{z^2} states are strongly coupled with softened out-of-plane modes by stretching σ bonds, resulting in high T_c SC, which would deepen our understanding of the important role of d_{z^2}-driven σ bond in the SC of transition metal boride. Furthermore, we consider the effect of pressure on the SC of the hP3 structure,

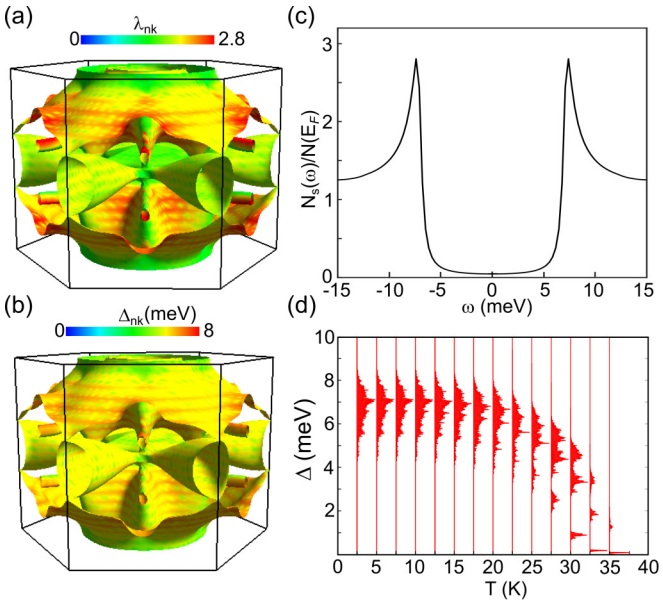

FIG. 4. Calculated k-resolved (a) EPC constant λ_{nk} and (b) superconducting gap Δ_{nk} (at 2.5 K) on the four FS sheets represented by the color scale. (c) The normalized quasiparticle DOSs at 2.5 K. (d) Energy distribution of the anisotropic superconducting gap Δ versus T for WB_2.

and the detailed results are shown in Figs. S2 and S3 of the Supplemental Material [33]. It is noted that with the increase in the pressure, the EPC parameters $\lambda_{q,v}$ and the obtained total EPC constants λ all get reduced. Accordingly, the values of estimated T_c get decreased and is ∼24 K at 150 GPa. Our further analysis reveals that the hardness of phonon vibration and reduction of the electron-phonon matrix element $M_{k,k+q}$ play key roles in the decrease in T_c, and the detailed discussion are shown in Fig. S3 of the Supplemental Material [33].

In the following, in order to reveal why there is weak EPC SC in the hP12 structure, we also calculate the electronic bonding and EPC properties to compare with those of the hP3 structure under 90 GPa. The hP12 structure has the space group of $P6_3/mmc$ with part of the B layers buckled [see Fig. 5(a)], and based on the crystal-field analysis (W site: D_{3d} point group), W d orbitals are splitted into a singlet a_{1g} (d_{z^2}) and a quartet e_g ($d_{x^2-y^2}$, d_{xy}, d_{xz}, and d_{yz}). Figures 5(c) and 5(d) display the calculated Pband and PDOS. It is noted that in both the hP12 and the hP3 structures, W d orbitals all have large electronic occupation, whereas, the difference is that for the hP12 structure, the d_{z^2} orbital has a small contribution to the states at E_F, and the other four d orbitals, i.e., the quartet e_g, exhibit larger electronic occupation. Especially, the d_{yz} orbital contribute most to Fermi surface states, and meanwhile, no VHS was observed in total DOS near E_F [see Fig. 5(d)]. We also plot the partial charge-density distribution in the range from the −0.1 to 0.1 eV as shown in Fig. 5(b), and it is seen that two neighboring W atoms are isolated without charge hybridization, indicating there are no the covalent bonds between neighboring W atoms in the hP12 structure. It is also verified by the calculated the integrated COHP with the positive value of 0.53 eV/pair [see Fig. 5(e)]. This result demonstrates that the difference in the point symmetries and

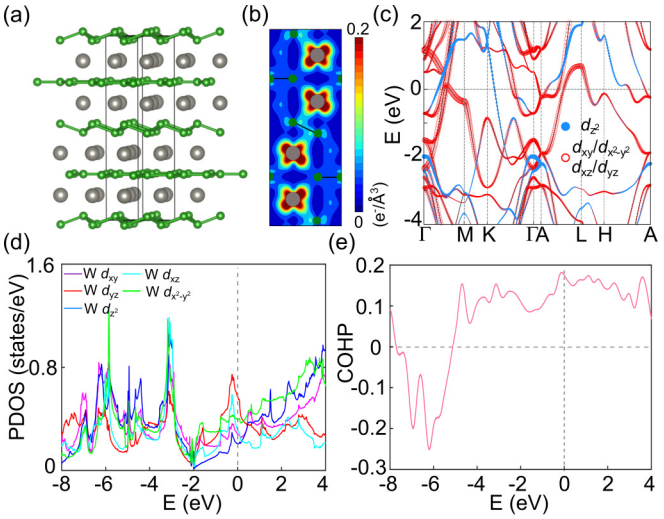

FIG. 5. (a) The side view of the hP12 structure under 90 GPa. (b) The calculated partial charge density. Calculated band structure (c) and partial DOS (d) with projected onto the atomic orbitals. (e) Total DOS associated with projected to W and B atoms.

crystal fields of W atoms between the hP3 and the hP12 structures give rise to the different orbital spilt, electronic distribution, and bonding nature, thereby yielding different SCs as discussed below.

These different electronic structures and bonding nature of the hP3 and hP12 structures reflect the different phonon vibrations and the EPC strength. From the atom-mode projected phonon spectra in Figs. 3(a) and 6(a), the similarity is that the low-frequency acoustic branches below 25 meV are dominated by the vibrations of W atoms, and the high-frequency parts arise from the vibrations of the B layers.

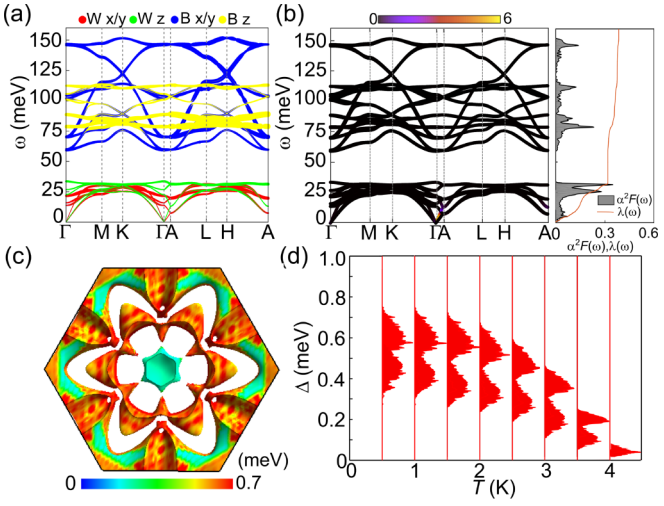

FIG. 6. (a) Phonon spectrum projected on atomic in-plane (x/y) and out-of-plane (z) vibrations. (b) Phonon spectrum with projection of EPC strength λ_{qv} using the color scale in the range of [0,6], and the isotropic Eliashberg function $\alpha^2F\omega$ with integrated EPC constant $\lambda(\omega)$. (c) Calculated k-resolved superconducting gap Δ_{nk} (at 1 K) on the FS sheets represented by the color scale. (d) Energy distribution of the anisotropic superconducting gap Δ versus T.

The difference is that for the hP12 structure, low-frequency acoustic branches including in-plane and out-of-plane modes all have very flat energetic dispersion, exhibiting atomlike vibrations. These stiffened phonon modes cannot effectively couple with the W d states of the FS, and thus, all acoustic modes have very small values of $\lambda_{q,v}$ as shown in the phonon spectrum with the projected $\lambda_{q,v}$ of Fig. 6(b). The obtained total EPC λ is only 0.36, much lower than $\lambda = 2.02$ of the hP3 structure, and accordingly, the states on the FS also produce smaller superconducting gap Δ_{nk} with the maximum value of ∼0.7 meV [see Fig. 6(c) and Fig. S4 of the Supplemental Material [33]]. As the increase in the temperature T, the value of the gap decreases to zero at the ∼4 K using $\mu^* = 0.13$, and the obtained T_c of the hP12 structure is 4 K [see Fig. 6(d)], close to previous report of $T_c = 1$ K [17,19]. Therefore, combining the electronic bonding and phononic properties of both the hP3 and the hP12 structures, it clearly shows that in the hP3 structure due to the hybridization of the d_{z^2} orbital, two W atoms are connected with a weak σ bond, and the W d_{z^2} states are strongly coupled with softened out-of-plane modes by stretching σ bonds, resulting in a large superconducting gap and, thus, high T_c. Although, in the hP12, the W atoms exist in isolation without charge hybridization between two neighboring W atoms, and accordingly their phonon modes are all very stiffened, which cannot effectively couple to their d orbital states, obtaining a small T_c. This result undoubtedly not only well explains why the hP3 could have strong EPC SC, but also points to the fact that although the hP3 WB_2 has essentially different electronic structures, bonding nature, and phonon vibrations with the isostructure MgB_2, both systems indeed reflect the similar superconducting nature that the metallic σ bonds can give rise to strong EPC SC. Additionally, we also study the electronic structures of the hP6 (space-group $P6_3/mmc$) and the hP3 ReB_2 (space-group $P6/mmm$), and find these are no d_{z^2}-driven σ covalent bonds in both structures [see Fig. S5 of the Supplemental Materials [33]], which may be able to explain why there is no SC in ReB_2. These findings would provide an important guidance to search for and design more high-T_c superconductors among transition metal borides by inducing covalent σ bonds between transition metals in the future research.

IV. SUMMARY

In conclusion, we have clearly displayed the different electronic bonding and phononic properties between the hP3 and the hP12 structures by the first-principles calculation, and reveal that the strong EPC SC in the hP3 originates from the strong coupling of the d_{z^2} states with the out-of-plane phonon modes by stretching σ bonds, whereas, in the hP12 structure, the stiffened phonon modes of the W atoms cannot effectively couple to the W d orbital states with T_c very low. Our findings not only could deepen our understanding of the microscopic mechanism of emergent strong EPC SC in hP3 WB_2, but also point out a route how to design more high-T_c superconductors among transition metal borides.

ACKNOWLEDGMENTS

This work was supported by the National Natural Science Foundation of China (Grants No. 12104129 and No. 12175079), and China Postdoctoral Science Foundation (Grant No. 2020M672201). The superconducting calculations were carried out in the National Supercomputing Center in Zhengzhou.

J.W. and M.W. contributed equally to this work.

[1] J. Nagamatsu, N. Nakagawa, T. Muranaka, Y. Zenitani, and J. Akimitsu, Superconductivity at 39 K in magnesium diboride, Nature (London) **410**, 63 (2001).

[2] J. M. An and W. E. Pickett, Superconductivity of MgB_2 : Covalent Bonds Driven Metallic, Phys. Rev. Lett. **86**, 4366 (2001).

[3] J. Kortus, I. I. Mazin, K. D. Belashchenko, V. P. Antropov, and L. L. Boyer, Superconductivity of Metallic Boron in MgB_2, Phys. Rev. Lett. **86**, 4656 (2001).

[4] H. J. Choi, D. Roundy, H. Sun, M. L. Cohen, and S. G. Louie, The origin of the anomalous superconducting properties of MgB_2, Nature (London) **418**, 758 (2002).

[5] Y. Kong, O. V. Dolgov, O. Jepsen, and O. K. Andersen, Electron-phonon interaction in the normal and superconducting states of MgB_2, Phys. Rev. B **64**, 020501(R) (2001).

[6] K.-P. Bohnen, R. Heid, and B. Renker, Phonon Dispersion and Electron-Phonon Coupling in MgB_2 and AlB_2, Phys. Rev. Lett. **86**, 5771 (2001).

[7] T. Yildirim, O. Glseren, J. W. Lynn, C. M. Brown, T. J. Udovic, Q. Huang, N. Rogado, K. A. Regan, M. A. Hayward, J. S. Slusky, T. He, M. K. Haas, P. Khalifah, K. Inumaru, and R. J. Cava, Giant Anharmonicity and Nonlinear Electron-Phonon Coupling in MgB_2: A Combined First-Principles Calculation and Neutron Scattering Study, Phys. Rev. Lett. **87**, 037001 (2001).

[8] A. Liu, I. I. Mazin, and J. Kortus, Beyond Eliashberg Superconductivity in MgB_2: Anharmonicity, Two-Phonon Scattering, and Multiple Gaps, Phys. Rev. Lett. **87**, 087005 (2001).

[9] J. Karpinski, N. Zhigadlo, S. Katrych, K. Rogacki, B. Batlogg, M. Tortello, and R. Puzniak, MgB_2 single crystals substituted with Li and with Li-C: Structural and superconducting properties, Phys. Rev. B **77**, 214507 (2008).

[10] I. Pallecchi, P. Brotto, C. Ferdeghini, M. Putti, A. Palenzona, P. Manfrinetti, A. G. Lehmann, A. Orecchini, C. Petrillo, F. Sacchetti, M. Affronte, G. Allodi, R. D. Renzi, S. Serventi, A. Andreone, G. Lamura, D. Daghero, R. S. Gonnelli, and M. Tortello, Investigation of Li-doped MgB_2, Supercond. Sci. Technol. **22**, 095014 (2009).

[11] Y. Feng, Y. Zhao, A. K. Pradhan, C. H. Cheng, J. K. F. Yau, L. Zhou, N. Koshizuka, and M. Murakami, Enhanced flux pinning in Zr-doped MgB_2 bulk superconductors prepared at ambient pressure, J. Appl. Phys. **92**, 2614 (2002).

[12] S. Kalavathi and C. Divakar, Superconductivity in dense $Mg1_{1-x}M_xB_2$ (M = Zr, Nb, Mo; x = 0.05) materials sintered under pressure, Bull. Mater. Sci. **28**, 249 (2005).

[13] H. J. Choi, S. G. Louie, and M. L. Cohen, Prediction of superconducting properties of CaB_2 using anisotropic eliashberg theory, Phys. Rev. B **80**, 064503 (2009).

[14] I. D. R. Mackinnon, P. C. Talbot, and J. A. Alarco, Phonon dispersion anomalies and superconductivity in metal substituted MgB_2, Comput. Mater. Sci. **130**, 191 (2017).

[15] C. Y. Pei, J. F. Zhang, Q. Wang, Y. Zhao, L. L. Gao, C. S. Gong, S. J. Tian, R. T. Luo, M. T. Li, W. G. Yang, Z. Y. Lu, H. C. Lei, K. Liu, and Y. P. Qi, Pressure-induced superconductivity at 32 K in MoB_2, Nat. Sci. Rev. **10**, nwad034 (2023).

[16] X. H. Liu, X. W. Huang, P. Song, C. Z. Wang, L. Y. Zhang, P. Lv, L. L. Liu, W. F. Zhang, J. H. Cho, and Y. Jia, Strong electron-phonon coupling superconductivity in compressed α-MoB_2 induced by double van hove singularities, Phys. Rev. B **106**, 064507 (2022).

[17] J. Lim, A. C. Hire, Y. Quan, J. S. Kim, S. R. Xie, S. Sinha, R. S. Kumar, D. Popov, C. Park, R. J. Hemley, Y. K. Vohra, J. J. Hamlin, R. G. Hennig, P. J. Hirschfeld and G. R. Stewart, Creating superconductivity in WB_2 through pressure-induced metastable planar defects, Nat. Commun. **13**, 7901 (2022).

[18] C. Y. Pei, J. F. Zhang, C. S. Gong, Q. Wang, L. L. Gao, Y. Zhao, S. J. Tian, W. Z. Cao, C. H. Li, Z. Y. Lu, H. C. Lei, K. Liu and Y. P. Qi, Distinct superconducting behaviors of pressurized WB_2 and ReB_2 with different local B layers, Sci. China Phys. Mech. Astron. **65**, 287412 (2022).

[19] S. R. Xie, Y. Quan, A. C. Hire, B. Deng, J. M. DeStefano, I. Salinas, U. S. Shah, L. Fanfarillo, J. Lim, J. Kim, G. R. Stewart, J. J. Hamlin, P. J. Hirschfeld and R. G. Hennig, Machine learning of superconducting critical temperature from eliashberg theory, npj Comput. Mater. **8**, 14 (2022).

[20] A. B. Migdal, Interaction between electrons and lattice vibrations in a normal metal, Sov. Phys. JETP **7**, 996 (1958).

[21] G. M. Eliashberg, Interaction between electrons and lattice vibrations in a superconductors, Sov. Phys. JETP **11**, 696 (1960).

[22] G. Kresse and J. J. Hafner, *Ab initio* molecular dynamics for open-shell transition metals, Phys. Rev. B **48**, 13115 (1993).

[23] G. Kresse and J. Furthmüller, efficiency of *ab-initio* total energy calculations for metals and semiconductors using a plane-wave basis set, Comput. Mater. Sci. **6**, 15 (1996).

[24] P. E. Blöchl, Projector augmented-wave method, Phys. Rev. B **50**, 17953 (1994).

[25] J. P. Perdew, K. Burke, and M. Ernzerhof, Generalized Gradient Approximation Made Simple, Phys. Rev. Lett. **77**, 3865 (1996).

[26] P. Giannozzi, S. Baroni, N. Bonini, M. Calandra, R. Car, C. Cavazzoni, D. Ceresoli, G. L. Chiarotti, M. Cococcioni, I. Dabo, A. Dal Corso, S. de Gironcoli, S. Fabris, G. Fratesi, R. Gebauer, U. Gerstmann, C. Gougoussis, A. Kokalj, M. Lazzeri, L. Martin-Samos, N. Marzari *et al.* QUANTUM ESPRESSO: A modular and open-source software project for quantum simulations of materials, J. Phys.: Condens. Matter **21**, 395502 (2009).

[27] M. Schlipf and F. Gygi, Optimization algorithm for the generation of ONCV pseudopotentials, Comput. Phys. Commun. **196**, 36 (2015).

[28] K. H. Lee, K. J. Chang, and M. L. Cohen, First-principles calculations of the coulomb pseudopotential μ^* : Application to Al, Phys. Rev. B **52**, 1425 (1995).

[29] P. Giannozzi, Jr., O. Andreussi, T. Brumme, O. Bunau, M. Buongiorno Nardelli, M. Calandra, R. Car, C. Cavazzoni, D. Ceresoli, M. Cococcion, N. Colonna, I. Carnimeo, A. Dal Corso, S. de Gironcoli, P. Delugas, R. A. DiStasio, Jr., A. Ferretti, A. Floris, G. Fratesi, G. Fugallo, R. Gebauer, U. Gerstmann, F. Giustino *et al.* Advanced capabilities for materials modelling with quantum ESPRESSO, J. Phys.: Condens. Matter **29**, 465901 (2017).

[30] R. Dronskowski and P. E. Blöchl, Crystal orbital hamilton populations (COHP). Energy-resolved visualization of chemical bonding in solids based on density-functional calculations, J. Phys. Chem. **97**, 8617 (1993).

[31] S. Maintz, V. L. Deringer, A. L. Tchougréeff, and R. Dronskowski, LOBSTER: A tool to extract chemical bonding from plane-wave based DFT, J. Comput. Chem. **37**, 1030 (2016).

[32] J. Hou, X. J. Weng, A. R. Oganov, X. Shao, G. Gao, X. Dong, H. Wang, Y. Tian, X. F. Zhou, Helium-nitrogen mixtures at high pressure, Phys. Rev. B **103**, L060102 (2021).

[33] See Supplemental Material at http://link.aps.org/supplemental/10.1103/PhysRevMaterials.7.074804 for calculated crystal orbital Hamiltonian population, superconducting properties of the hP3 structure at different pressures, electronic structures of ReB_2, which includes Refs. [34–37].

[34] A. A. Mostofi, J. R. Yates, Y. S. Lee, I. Souza, D. Vanderbilt, and N. Marzari, wannier90: A tool for obtaining maximally-localised wannier functions, Comput. Phys. Commun. **178**, 685 (2008).

[35] P. B. Allen and B. Mitrović, in *Solid State Physics*, edited by H. Ehrenreich, F. Seitz, and D. Turnbull (Academic, New York, 1982), Vol. 32, p. 1.

[36] G. Grimvall, *The Electron-Phonon Interaction in Metals* (North-Holland, New York, 1981).

[37] P. B. Allen, in *Dynamical Properties of Solids*, edited by G. K. Horton and A. A. Maradudin (North-Holland, Amsterdam, 1980), Vol. 3, p. 95.

[38] S. Baroni, S. de Gironcoli, A. Dal Corso, and P. Giannozzi, Phonons and related crystal properties from density-functional perturbation theory, Rev. Mod. Phys. **73**, 515 (2001).

[39] F. S. Khan and P. B. Allen, Deformation potentials and electron-phonon scattering: Two new theorems, Phys. Rev. B **29**, 3341 (1984).

[40] W. L. McMillan, Transition temperature of strong-coupled superconductors, Phys. Rev. **167**, 331 (1968).

[41] E. R. Margine and F. Giustino, Anisotropic migdal-eliashberg theory using wannier functions, Phys. Rev. B **87**, 024505 (2013).